

The Parker Instability in 3-D: Corrugations and Superclouds Along the Carina-Sagittarius Arm

José Franco¹, Jongsoo Kim², Emilio J. Alfaro³ and Seung Soo Hong⁴

Received _____; accepted _____

¹Instituto de Astronomía, Universidad Nacional Autónoma de México, Apdo. Postal 70-264, 04510 México D. F., México; pepe@astrocu.unam.mx

²Korea Astronomy Observatory, 61-1, Hwaam-Dong, Yusong-Ku, Taejon 305-348, Korea; jskim@kao.re.kr

³Instituto de Astrofísica de Andalucía CSIC, Apdo. 3004, Granada 18080, Spain; emilio@iaa.es

⁴Department of Astronomy, Seoul National University, Seoul 151-742, Korea; sshong@astroism.snu.ac.kr

ABSTRACT

Here we present three-dimensional MHD models for the Parker instability in a thick magnetized disk, including the presence of a spiral arm. The B -field is assumed parallel to the arm, and the model results are applied to the optical segment of the Carina-Sagittarius arm. The characteristic features of the undular and interchange modes are clearly apparent in the simulations. The interchange mode appears first and generates small interstellar structures in the inter-arm regions, but its development inside the arm is hampered by the acceleration of the spiral wave. In contrast, the undular mode follows its normal evolution inside the spiral wave, creating large gas concentrations distributed along the arm. This results in a clear arm/inter-arm difference: the instability triggers the formation of large interstellar clouds (with masses in the range of 10^6 to $10^7 M_{\odot}$) inside the arms, but generates only small structures with slight density enhancements in the inter-arm regions. The resulting clouds are distributed in an antisymmetric way with respect to the midplane, and their masses are similar to those inferred for HI superclouds in our Galaxy. Such a cloud distribution results in an azimuthal corrugation along the arm and, for conditions similar to those of the optical segment of the Carina-Sagittarius arm, it has a wavelength of about 2.4 kpc. This structuring, then, can explain the origin of both HI superclouds and the azimuthal corrugations in spiral arms. In particular, the wavelength of the fastest growing undular mode matches the corrugation length derived with the young stellar groups located in the optical segment of the Carina-Sagittarius arm.

Subject headings: Galaxy: kinematics and dynamics — Galaxy: structure — Instabilities — ISM: clouds — ISM: magnetic fields — ISM: structure — MHD

1. INTRODUCTION

The gaseous disk of the Milky Way is a magnetized medium with a variety of different components, some of them extending for a few hundred parsecs above the midplane (see Boulares & Cox 1990). It has a very complex structure, with atomic and molecular clouds threaded by magnetic fields and embedded in a more diffuse and ionized medium. Also, the gas of the disk is continuously perturbed by a number of different agents. These range from well defined and localized energy perturbations, such as expanding HII regions and supernova explosions, to large scale shocks driven by spiral waves (or by global perturbations induced by interactions with nearby neighbors). The magnetic field provides partial support to the extended disk layers (and allows for an efficient energy and momentum exchange between different parts of the disk), but also induces large scale instabilities, as discussed several decades ago by Parker (1966, 1967). When a relatively well ordered B -field is present, the compression generated by a strong perturbation (say, a spiral wave) changes the magnetic field downstream and the gas driven by the distorted field lines accumulates large mass clouds along the valleys in the field lines. This is called the “Parker” instability and, as in the case of gravitational instabilities, it may also gather giant cloud complexes in spiral arms (*e.g.* Mouschovias *et al.* 1974; Shu 1974; Elmegreen & Elmegreen 1986). Obviously, these type of instabilities can be triggered by a variety of different perturbations (*e.g.* Franco *et al.* 1995; Hanasz & Lesch 2000), and a two-dimensional (2-D) analysis of the terms driving separate instabilities in a sheared disk (*i.e.*, thermal, gravitational, and Parker) has been reviewed by Elmegreen (1992,1993). More recently, with a 3-D model of the Parker instability in a thin disk and under a uniform gravity, the actual possibility of forming large cloud complexes via this instability has been questioned (*e.g.* Kim *et al.* 1998), but a more detailed study with a realistic galactic disk model in 3-D is now needed. This is indeed important because our Galaxy has a thick, multi-component gaseous disk with a relatively strong magnetic field that extends more than a kiloparsec above the plane

of the disk (*e.g.* Boulares & Cox 1990; Beck et al. 1996). In contrast with previous thin disk models, the presence of these extended magnetized components change the response of the general interstellar medium to perturbations (*e.g.* Martos & Cox 1998; Martos *et al.* 1999; Santillán *et al.* 1999).

The first steps in this direction, including a multicomponent model for the gaseous disk and the observed gravitational field in the solar neighborhood, have been done by Kim *et al.* (2000; hereafter Paper I) and Santillán *et al.* (2000; hereafter Paper II). They performed a 2-D linear stability analysis, with the corresponding MHD models, and found that the wavelengths and time scales for the Parker instability are strongly modified. The most unstable undular mode in the Solar circle has a wavelength of about 3 kpc and an e-folding time of $\sim 3 \times 10^7$ yr (significantly larger than those derived for thin disk cases; see Kim & Hong 1998). The 2-D MHD experiments confirm these results and show, in addition, that the preferred parity of the instability is antisymmetrical (*i.e.*, the resulting condensations are distributed above and below the midplane). Thus, one signature of the undular mode is a corrugation pattern along the direction of the original B -field.

The existence of corrugations along spiral arms has been discussed in the literature by several authors, and perhaps the best studied case is the Carina-Sagittarius arm. There are several important problems in deriving the precise location and properties of spiral arms in the Milky Way (see discussions by Liszt 1985 and Roberts & Burton 1997), and most properties of spiral structure are better studied in external galaxies. Nonetheless, even when its detailed properties are not completely established, the Carina-Sagittarius arm is one of the most conspicuous and best studied spiral arms in our Galaxy. According to present estimates, it circles for about 40 kpc around the galactic center, and follows a logarithmic spiral curve with a pitch angle of $\sim 10^\circ$, close to the one expected from the density wave theory (*e.g.* Grabelsky *et al.* 1988). The wavy vertical distribution of large clouds along

Carina-Sagittarius unveils an azimuthal corrugation pattern that seems to be present in other arms of our Galaxy (Spicker & Feitzinger 1986). Such a pattern is also apparent in the distribution of young stellar clusters within the arm (Alfaro *et al.* 1992a). In contrast, the existence of azimuthal wavy structuring has not been reported for the inter-arm regions. It is unclear, however, if this is simply due to observational restrictions (*i.e.*, due to a smaller amount of gaseous features and young stellar tracers) or to a real lack of structuring.

With all these restrictions in mind, here we explore the features that appear in 3-D models for the Parker instability operating inside the arms. The instability has two independent modes, undular and interchange, with different properties and wavelengths (see Hughes & Cattaneo 1987). The undular mode, which is the best studied branch of the instability, is a 2-D event that evolves in the plane defined by the gravitational acceleration and the original direction of the B -field. It deforms the magnetic field lines, and creates large gas condensations distributed in an antisymmetric fashion with respect to the midplane. Such an arrangement gives the impression of a corrugated system, with a corrugation length equal to the wavelength of the fastest growing mode. The interchange mode, on the other hand, operates outside the plane of the undular mode and allows for the vertical exchange of field lines. In 3-D, both modes combine into a mixed mode, creating a more complex network of condensations. However, some of the features generated by the pure undular mode can persist in the non-linear 3-D regime, but the resulting gas structures are more filamentary (Kim *et al.* 1998; Kim, Ryu & Jones 2001). Thus, as long as the undular structure is not washed away by the action of the interchange mode in 3-D, the structuring observed along spiral arms may well be explained by this instability. As pointed out by Beck *et al.* (1989), this is also a potential mechanism to create the periodic variations observed in the B -field of the southwestern arm of M31.

In this paper we show that this is indeed the case, and report the results of 3-D

magneto-hydrodynamical simulations of the Parker instability in a thick disk including the presence of a spiral wave. The model is performed with parameters appropriate for the optical segment of Carina-Sagittarius, the best studied region of this arm. The presence of the spiral wave is modeled as a perturbation in the gravitational field. The interchange mode appears at early times but the acceleration of the spiral wave, even when small compared with the disk gravity, effectively quenches its further development inside the arm. Hence, the undular mode ends up dominating the evolution inside the spiral wave, and creates major gas condensations along the arm. These condensations are distributed in an antisymmetric way with respect to the midplane, and with a wavelength of about 2.4 kpc, similar to the corrugation length derived by Alfaro *et al.* (1992a) and Berdnikov & Efremov (1993). The organization of the paper is as follows. Section 2 describes the 3-D models and results. Section 3 presents an overview of the observed properties of the Carina-Sagittarius Arm, and Section 4 presents a brief discussion of the results.

2. Three-Dimensional Models

2.1. The Model Galaxy

The details of the multi-component thick disk model for the Solar circle (*i.e.*, the observed disk gravity and gas density stratifications near the Sun) are described in Papers I and II. Here we use the same model but scale the disk parameters to those of the optical segment of Carina-Sagittarius (see next Section). This is perhaps the best known region of the arm and is located inside the solar circle at galactocentric radii between $R/R_0 \sim 0.8 - 0.9$, where $R_0 \sim 8.5$ kpc is the radius of the Solar circle. As stated before, Carina-Sagittarius has a total extension of about 40 kpc, and covers a wide range of galactocentric radii, from about 5 to 12 kpc (these values are corrected for the location of the Sun; see Fig. 4 in Grabelsky *et al.* 1988). Given that the scale height and midplane density of the gaseous disk

vary with galactocentric distance, the average value of these parameters change by about 40% along the radial extent of this arm (see Malhotra 1994). Using the radial distributions of molecular and atomic gas in our Galaxy reported by Malhotra (1994, 1995), the midplane density at the location of the optical segment increases by 20-30 % with respect to the Solar circle, whereas the HI scale height decreases by a similar amount. Also, the gravitational acceleration of the disk at these locations is increased by 25 %.

A brief summary of the magnetic field in our Galaxy is given in the next section, and here we assume a well ordered field, with a midplane strength of $B(0) = 5 \mu\text{G}$, that runs parallel to the spiral arm (see Beck *et al.* 1996; Heiles 1996; Indrani & Deshpande 1998; Vallee 1998). The spiral density wave representing the arm is modeled as a perturbation in the gravitational field, following the elliptical approximation described by Martos & Cox (1998). This perturbation, which has a maximum amplitude of 5% of the gravitational field of the disk, is an ellipse centered in the $x - z$ plane, and goes to zero in a distance of 1 kpc along the x -direction and 0.6 kpc along the z -direction.

In summary, we use the z -distributions described in Papers I and II with some modifications: the gas density is increased by 25 % ($n_0 = 1.4 \text{ cm}^{-3}$), the effective scale height is decreased by 20 % ($H_{\text{eff}} = 133 \text{ pc}$), and the gravitational acceleration is increased by 25 %. An additional 5 % gravitational perturbation is then added at the location of the arm. All gas layers are assumed isothermal, with a sound speed of $c_s = 8.4 \text{ km s}^{-1}$. The basic time unit is $H_{\text{eff}}/c_s \sim 1.54 \times 10^7 \text{ yr}$ and, unless stated otherwise, all times are given in this unit. This disk is Parker unstable and the resulting most unstable perturbation for the undular mode, derived with the method described in Paper I, has a wavelength of $\sim 2.4 \text{ kpc}$ and its e-folding time is $\sim 3 \times 10^7 \text{ yr}$.

The models are performed with the isothermal MHD TVD code described by Kim *et al.* (1999) in a Cartesian coordinate system, (x, y, z) , with a 128^3 zone grid. The frame of

reference is at rest with the spiral wave and, for simplicity, the gas has no relative motion with respect to the spiral arm. The physical size of the computational cube is $(4 \text{ kpc})^3$, and the linear resolution of the models is about 32 pc. The spiral arm is oriented along the y -axis, and the z -axis is perpendicular to the midplane (the initial B -field direction, then, is also along the y -axis). Galactic differential rotation and self-gravity are not included, and we restrict the study to the structures formed during time scales of the order of several times 10^8 yr.

For the initial setup, as described in Paper II, the unperturbed disk is set in magnetohydrostatic equilibrium at $t = 0$. Then, the acceleration of the spiral wave is introduced in the x and z directions of the computational domain and, to generate a perturbation in the y -axis, an additional velocity perturbation is also introduced at this moment. We made a series of runs with different types of perturbations, including random and sinusoidal velocity fields, and with several initial amplitudes (ranging from 10^{-4} to $10^{-1} c_s$). The spiral wave and the velocity perturbations, then, represent the seeds that trigger the instability.

2.2. Results

Figure 1 shows the evolution of the rms gas velocity components ($\langle v_x^2 \rangle^{1/2}$, $\langle v_y^2 \rangle^{1/2}$, and $\langle v_z^2 \rangle^{1/2}$) for the run with a random velocity perturbation and with an initial amplitude of $10^{-4} c_s$. The solid line has a slope equal to the growth rate of the fastest growing undular mode. The gas motions along the y -direction are not affected by the gravitational acceleration of the spiral wave and, except for a short period at very early times (*i.e.*, $t \leq 10$), the evolution of v_y follows the track expected for the undular mode (see Paper II). In contrast, the motions along the other two directions are continuously modified by the acceleration of the arm, and the evolution of v_x and v_z follow different growth rates

up to $t \sim 20$. At about $t = 25$, all three velocity components reach a maximum value and then decline with smooth oscillations at later times. Thus, the evolution can be divided into the three stages of the instability (linear, non-linear, and final equilibrium) described in Paper II. The initial linear stage lasts up to about $t = 20$, and the non-linear saturated stage can be defined up to about $t \sim 40$. The system enters into the final equilibrium (or damping oscillatory) stage after this time. These same features also appear in the rest of the runs with sinusoidal perturbations, and they only differ in the timescales at which the different stages are initiated (for sinusoidal perturbations with larger initial amplitudes, the linear stage starts and gets saturated at earlier times).

Figure 2 shows snapshots of the density structures, velocity fields, and magnetic field topologies at three selected times. To simplify the visualization of the 3-D data cubes, the densities and velocities are shown for the central $x - z$ plane only, and the B -field lines are shown only near the central $y - z$ plane. In addition, to provide a better idea of the 3-D structuring, two isodensity surfaces (with the same reference value $n = 0.04 \text{ cm}^{-3}$) are also included in the snapshots. The velocity fields are represented with red arrows (the value of the unit arrow is rescaled at each time frame), and the B -field lines are shown in blue. The densities are color-coded from red to purple, as the value decreases. To complete the information, Figure 3 shows the corresponding $x - y$ maps of the gas column density, integrated along the z -axis, at the same three selected times. The vertical column densities at these three epochs are normalized with the initial column density, $1.1 \times 10^{21} \text{ cm}^{-2}$, which is obtained by integrating the initial density distribution from -2 kpc to +2 kpc (see, equation 5 in Paper II). As explained in the previous section, we have adjusted the midplane density and scale height of the gas to the values in the Carina-Sagittarius region. The resulting total column density, however, is the same as that of the solar neighborhood.

Once the spiral and random perturbations are introduced, the initial magnetohydrostatic

equilibrium is broken and the system begins to oscillate. The first frames of Figs. 2 and 3, at $t = 15$, illustrate the evolution at the early stages of the instability, during the linear growth. Given that the volume and column densities are increased by the acceleration of the spiral wave, the location of the arm is clearly seen in both frames. The B -field shows small undulations, the isodensity surfaces are only mildly distorted, and the gas velocities at high latitudes are being amplified. The second frames, at $t = 25$, show the evolution near the end of the linear stage. The B -field lines are now clearly twisted and strongly undulated by the combined action of the undular and interchange modes (this is, by the mixed mode). The interchange mode, which has the shorter wavelengths and fastest growing rates, creates small structures during the early stages, and the isodensity surfaces are completely deformed by the presence of several small clumps. These are best seen in the column density map of Fig. 3, which shows that the early structures are in general small, but the smaller ones appear mainly in the inter-arm regions. This in turn indicates that the arm acceleration along the x -direction effectively quenches the further growth of the interchange mode (which otherwise would be slicing the computational domain into thin filamentary structures). The effect appears in models including the self-gravity of the gas (*e.g.* Lee & Hong 2001). Hence, at later times, the regions inside the spiral arm are mainly subject to the undular mode, but the inter-arm regions follow the mixed mode with the combined undular and interchange branches. This is illustrated in the third frames in Figs. 2 and 3, at $t = 32$, with the evolution at the non-linear saturated stage. There are four main condensations located along the arm, and separated by distances between 1 and 1.3 kpc. They are positioned at the valleys of the wavy B -field lines, indicating that the undular mode is dominating the evolution along the arm. As time passes by, the condensations continue to accumulate mass, increasing their sizes and peak densities, but the results for times larger than $t \sim 30$ (which corresponds to $\sim 5 \times 10^8$ yr) are probably not relevant for actual applications to our Galaxy. From the third frame of Fig. 3, then, we estimate the

masses of the largest and smallest condensations (centered at $x = 0.0$ kpc and $y = -0.4$ kpc, and $x = 0.2$ kpc and $y = 0.4$ kpc, respectively) by integrating inside column densities that are 1.5 times above the initial value, $1.1 \times 10^{21} \text{ cm}^{-2}$. Assuming a 10% number ratio of helium to hydrogen, the resulting masses are $2.9 \times 10^6 M_{\odot}$ for the small condensation, and $9.0 \times 10^6 M_{\odot}$ for the large one.

Figure 4a shows the mid-plane density map at $t = 32$, along with a cubic polynomial fitting curve that passes through the main density peaks. The map shows the same features that appear in the third frame of Fig. 3, indicating that the structuring in the column density is mainly determined by the structuring near the midplane. In order to see better the vertical distribution of these density peaks, Fig. 4b shows the vertical distribution of the density along the fitting curve. This panel clearly shows the corrugation pattern, where the density peaks are positioned alternatively above and below the mid-plane. Figures 5a and 5b show the magnetic field structure near the central $y - z$ plane and near the central $x - y$ plane, respectively. Also, we show the isodensity surfaces with 0.8 times the initial value, which provide a clear visual impression of the relative location of the main gas concentrations.

Finally, Figure 6 shows the z -velocity component of the gas concentrations along the arm. The Figure displays a position-velocity map for the arm at $t = 32$, as seen from the north galactic pole. This corresponds to the expected gas velocity structure that may appear along the spiral arms in face-on galaxies. Given the restrictions of the present 3-D simulations in a Cartesian grid (*i.e.*, a single fluid at rest with the arm and without self-gravity, differential rotation, random B -fields, etc.), we cannot properly address the details of the gas motions in the $x - y$ plane and restrict the kinematic information of the model to the z -velocity components of the condensations. Thus, this figure provides an important observable signature of the process, and represents one of the main possible

links between CO and HI observations and the present stage of the simulations.

3. Corrugations, Spacings, and Superclouds

3.1. The Carina-Sagittarius Arm

The evidence that Carina-Sagittarius is truly a major spiral arm was discussed by Cohen *et al.* (1985) and Grabelsky *et al.* (1988), who delineated its location from the distribution of molecular clouds in the first and fourth galactic quadrants. Additional studies with different galactic tracers (*i.e.*, including HI clouds, HII regions, and young stellar objects; see Alfaro *et al.* 1992a,b and references therein) support the idea that the optical segments of Carina and Sagittarius are indeed part of the same major spiral arm. Thus, this arm is our best local probe for the spiral structure of the Milky Way, and for the distribution and spacing of gas clouds (and star forming centers) along the arms.

The azimuthal corrugations along this arm have been observed in both the stellar and gas components. The corrugation pattern reported by Alfaro *et al.* (1992a) is outlined by open clusters located in the optical segment of the arm (the closest region to the Sun, at $R/R_0 \sim 0.8 - 0.9$). The resulting wavelength (*i.e.*, the distance between two consecutive maxima or minima of the vertical deviations along the arm) is 2.4 kpc, and is about twice the value of the separation between the complexes delineated by Cepheid stars (Berdnikov & Efremov 1993) and young clusters (Avedisova 1989). This is also twice the average distance of the “shingle-like” structures delineated, with the aid of wide-angle photographs and photoelectric surface photometry, by star-forming regions in this spiral arm, 1.2 kpc (Schmidt-Kaler & Schlosser (1973). This structuring was derived almost three decades ago with lower quality data (and, as correctly stated by an anonymous referee, it could now be repeated with much better optical, infrared, radio, and extinction data), but it is interesting

to notice that it is consistent with more recent results obtained with other tracers.

In the case of the gas, there are determinations of the azimuthal corrugation scales for all known Galactic arms (Spicker & Feitzinger 1986). This seems to indicate that they are common features of spiral arms, but this is a difficult study and the resulting wavelength values are less accurate than those estimated for stellar clusters. Moreover, the derived wavelengths depend on the tracer used, and there are three main values reported for the Sagittarius arm: the shorter value (derived from OB groups and HII regions) is between 1 and 2 kpc, the second one is between 4 and 8 kpc, and the large scale value (obtained from HI data in the interval $l = 30^\circ - 60^\circ$) has an upper limit of 13.6 kpc (Schmidt-Kaler & Schlosser 1973; Spicker & Feitzinger 1986). This variety of different scale lengths may be indicative that, aside from possible errors in several of these estimates, a number of different wavelengths could be coexisting in the arms, or that the corrugation length varies with galactocentric distance. Due to obvious extinction problems, the larger scales cannot be confirmed with stellar data, but the shorter length is about a half of the wavelength derived by Alfaro *et al.* for open clusters (again, more sensitive HI and CO data are now available, and interferometric HI data will soon be available, that could be used in a new analysis of gas corrugations along spiral arms).

Summarizing these results, the present observational evidence indicates that azimuthal corrugations are probably common features in spiral arms. The spacings between clouds, or young stellar groups, are probably associated with these corrugation wavelengths. In particular, for the optical segment of the Carina-Sagittarius arm, the corrugation length is 2.4 kpc. This value is coincidental with the wavelength derived in this study for the fastest growing mode of the undular branch of the Parker instability.

3.2. Superclouds

In a closely related type of study, Efremov (1998) made an analysis of the spacings between “HI superclouds” in Carina-Sagittarius. These are large atomic hydrogen clouds, with masses between 10^6 and $4 \times 10^7 M_\odot$ and average particle densities between 3 and 20 cm^{-3} . They seem to be gravitationally bounded and contain giant molecular complexes, and their molecular fraction decreases with increasing galactocentric distance. Also, they are found in spiral arms (Elmegreen & Elmegreen 1987), but there are at least a couple of large clouds in our Galaxy that may belong to this category and are not clearly inside a spiral arm (G216-2.5 in the outer Galaxy, and G2817+0.05 in the inner Galaxy. Their masses are close to $10^6 M_\odot$, the lower mass limit for superclouds; see Maddalena & Thaddeus 1985; Williams & Maddalena 1996; Minter *et al.* 2001)).

Efremov found a bimodal distribution in the spacing of these clouds, and the two peaks are centered around the values $0.1R_0$ and $0.2R_0$. He noted that this type of distribution also appears in other spirals such as NGC 1365, NGC 2395 and NGC 613 (Elmegreen & Elmegreen 1983). The shorter scales seem to be associated with inner galactic regions, while the outer segments of the arms show larger average separations. This is more evident along the segment in the first galactic quadrant, where the HI superclouds are separated by shorter distances (Elmegreen & Elmegreen 1987). A similar study in a sample of spiral galaxies by Elmegreen & Elmegreen (1983), shows that the spacings of giant HII regions and superclouds depends on the size of the host galaxy: the typical distance (L) between adjacent star-forming regions scales linearly with the photometric radius (R_{25}) of the galaxy, $L \sim 0.23R_{25}$. Taking $R_{25} = 10 \text{ kpc}$ for our Galaxy (de Vaucouleurs 1979), the corresponding mean distance between giant HII regions along the arms is 2.3 kpc. This value agrees with the second peak value found by Efremov and is very close to the corrugation length found by Alfaro *et al.* (1992a). This latter coincidence may be only fortuitous, but the spacings

and masses of superclouds are certainly similar to those obtained in our model.

3.3. Magnetic Fields

The ordered component of the magnetic field in the disk of the Milky Way, and external spirals, have both radial and azimuthal components (see Beck *et al.* 1996; Valle 1998; Beck 2001). Many details of the field structure are still poorly known, but the field of the disk extends to high-galactic latitudes and displays several reversals both inside and outside the Solar circle. The strength of the local regular field is between 3 and 5 μG (the total field strength near the Sun is 4 – 8 μG , and this value increases by about 50% at 3 kpc from the Galactic center). The azimuthal field pattern runs nearly parallel to the spiral arms, but the pitch angles of the "magnetic arms" are probably smaller than those derived for the arms in gas and stars. Actually, the stellar and gaseous arms observed in infrared and optical pictures of external galaxies do not always coincide, and in some cases they are very different (for instance, NGC 309 is a multi-arm spiral in the optical, but is a barred spiral with two-arms in the infrared; see chapter 5 of Bertin & Lin 1996). Some of these differences are also apparent in the magnetic arms of a number of external galaxies, where the field maxima do not coincide with the locations of the optical arms. Despite these differences, however, the ordered fields are always aligned almost parallel to the spiral arms, and can reach average strength values of up to 20 μG (see Beck *et al.* 1996).

In the case of M31, the magnetic field shows a ring-like structure at a radius of about 10 kpc from the center, that follows the CO and dust emission from the arms (see Beck 2000). The alignment is very clear in the whole ring and suggests that the B -field is anchored in the gaseous clouds of the arms. The regular field, then, runs along the arm but it also shows systematic fluctuations around the mean orientation (Beck *et al.* 1989). These fluctuations, which have a conspicuous arc-like pattern, indicate azimuthal corrugations in the magnetic

field along the arm, with a scale length of about 4.5 kpc. Thus, the corrugation pattern is also apparent in the B -fields of the 10 kpc ring in M31, and the observed arc-like structures are similar to those obtained in our model (see Figure 4d).

4. Discussion

Here we have presented 3-D models of the Parker instability including the presence of a spiral wave. We assume a magnetized, isothermal thick disk model that is Parker unstable, with parameters appropriate for the optical segment of the Carina-Sagittarius arm. The spiral wave is treated as a perturbation in the gravitational field, and the initial B -field lines are oriented parallel to the spiral arm. The wavelength of the resulting fastest growing mode along the arm is about 2.4 kpc, very similar to the corrugation distance derived by Alfaro *et al.* (1992a). The corresponding growth time scales are about 3×10^7 year. These values are only 20 % smaller than those derived for the Solar circle (Paper I), but the most relevant outcome of this study is the role played by the instability in structuring the spiral arm.

The principal results of the 3-D models are: (i) The presence of the spiral wave effectively quenches the development of the interchange mode. Thus, the regions inside the arm are dominated by the undular mode, while the inter-arm regions are subject to the mixed mode. (ii) As the undular mode grows along the arm, mass gathering in the magnetic valleys creates large gas condensations. (iii) The final result of the instability is an antisymmetric distribution of large clouds along the arm, and smaller scale interstellar structures in the inter-arm regions. (iv) The z -component of the velocity field along the arm is also undulated, with an amplitude of about 10 km/s.

The main gas condensations, with masses within $10^6 - 10^7 M_\odot$, have properties similar

to those of the HI superclouds described by Elmegreen & Elmegreen (1987). They are in the correct mass range and, also, are formed from the diffuse HI medium located along the spiral arms. Our model indicates that, regardless of the presence of large scale gravitational instabilities in sheared magnetized regions (as have been discussed by Elmegreen 1987), these HI superclouds can be formed by the undular mode inside the arm. A logical consequence of this mechanism is that the resulting HI superclouds are mainly located along spiral arms. These clouds are natural seeds for the subsequent formation of giant molecular complexes, which can be formed in the central cloud regions, and are arranged in an antisymmetric fashion with respect to the midplane. We are currently performing 2-D simulations including the formation of molecular hydrogen, that indicate that this is certainly the case. The spacings of these clouds and their corresponding star-forming regions, then, should be a half of the wavelength of the fastest growing undular mode. For the conditions of the optical segment of the Carina-Sagittarius arm, this is about 1.2 kpc, very similar to the observed spacings of gaseous features and HII regions. This also gives support to the idea presented by Beck *et al.* (1989) that the corrugations of the B -field in M31, with length scales of about 4.5 kpc, may be due to the Parker-Jeans instability. One obvious corollary is that, given that the wavelength of the most unstable perturbation depends on the disk parameters, the spacings and corrugation lengths should vary with galactocentric distance.

Self-gravity, differential rotation, randomly oriented B -fields, cosmic rays, and the gas flow through the arm were not included in this first work. These effects are important but they are difficult to include, with our present resources and in a self-consistent manner, in a thick gaseous disk with a spiral wave. Some hints from previous studies, however, can be used to illustrate their possible influence. For instance, the spiral wave rotates as a rigid body and the shear due to differential rotation will affect mainly the inter-arm regions. In addition, the 3-D results with rotation discussed by Kim, Ryu & Jones (2001) indicate that

the inter-arm structures will be more affected and may become filamentary. Cosmic rays, on the other hand, will supply buoyancy to the magnetic tubes, reducing the time scales for the growth of the undular mode (*e.g.* Hanasz & Lesch 2000). Another effect is that raising magnetic loops will be twisted by differential rotation, leading to reconnection and dynamo action at a certain height. Also, as discussed by Elmegreen (1987) for gravitational instabilities, the magnetic field transfers angular momentum in a sheared disk and reduces the effects of differential rotation. These issues require further higher resolution studies including the effects of randomly oriented B -fields, that also modify the growth and wavelengths of the interchange mode (a random component strongly reduces the growth of this mode; Kim & Ryu 2001). Self-gravity, on the other hand, increases the growth rate of the undular instability but the combined Jeans-Parker instability does not change the wavelength of the most unstable mode (Elmegreen 1982a,b; Chow *et al.* 2000; Lee & Hong 2001). This will speed up the process, and will also lead to more compact and denser condensations inside the arm. Another very interesting and important effect discussed by Masset & Tagger (1996, 1997) is the possible exchange of waves between the gaseous and stellar disks that, aside from exciting warps, can also lead to corrugations. The inclusion of these effects, then, will tend to increase the contrast between arm and inter-arm regions, but will not change the basic conclusion of this study. Further observational and theoretical studies addressing these issues will shed more light on these important questions. In particular, forthcoming high-resolution studies of the atomic and molecular gas components of our Galaxy, such as the BU-FCRAO Galactic Ring Survey (*i.e.*, Simon *et al.* 2001; Jackson *et al.* 2001), will provide maps of the Carina-Sagittarius arm in great detail.

It is a big pleasure to thank Don Cox, Marco Martos, Frédéric Masset, Alfredo Santillán, and Michel Tagger for stimulating and informative discussions during the development of this project. We thank Rainer Beck for information about the B -fields in

spirals. We also thank the comments and questions made by the referee, that helped us to clarify the presentation. We are grateful to the Guillermo Haro Program of INAOE for hosting a magnificent workshop on the Dynamics of Disk Galaxies, where part of the present study was performed. This work has been partially supported by bilateral agreements between CONACYT-Mexico with KOSEF-Korea and CSIC-Spain. JF thanks the Instituto de Astrofísica de Andalucía and Seoul National University for their warm hospitality, and acknowledges partial support by DGAPA-UNAM grant IN118401 and by a R&D CRAY Research grant. JK also acknowledges the warm hospitality of the Instituto de Astronomía-UNAM. The work of SSH was supported in part by a grant from the Korea Research Foundation made in the year 1997. EJA acknowledges the hospitality of the Instituto de Astronomía-UNAM, and partial support from DGICYT through grants PB97-1438-C02-02 and by the Research and Education Council of the Autonomous Government of Andalucía (Spain).

REFERENCES

- Alfaro, E. J., Cabrera-Caño, J., & Delgado, A. J. 1992a, *ApJ*, 399, 576
- Alfaro, E. J., Delgado, A. J, & Cabrera-Caño, J. 1992b, *ApJ*, 386, L47
- Avedisova, V. S. 1989, *Astrophysics*, 30, 83
- Beck, R. 2000, in *The Interstellar Medium in M31 and M33*, ed. Berkhuijsen, E.M., Beck, R. & Walterbos, R.A.M., (Shaker: Aachen), 171
- Beck, R. 2001, *Space Sc. Rev.*, in press
- Beck, R., Brandenburg, A., Moss, D., Shukurov, A., & Sokoloff, D. 1996, *ARA&A*, 34, 155
- Beck, R., Loiseau, N., Hummel, E., Berkhuijsen, E. M., Gräve, R., & Wielebinski, R. 1989, *A&A*, 222, 58
- Berdnikov, L. N., & Efremov, Yu. N. 1993, *Astron. Lett.*, 19, 389
- Bertin, G. & Lin, C. C. 1996, *Spiral Structure in Galaxies: A Density Wave Theory*, (Cambridge: MIT Press)
- Boulares, A., & Cox, D. P. 1990, *ApJ*, 365, 544
- Chow, W., Matsumoto, R., Tajima, T., Umekawa, M. & Shibata, K. 2000, *ApJ*, 538, 710
- Cohen, R. S., Grabelsky, D. A., May, J., Bronfman, L., Alvarez, H., & Thaddeus, P. 1985, *ApJ*, 290, L15
- de Vaucouleurs, G. 1979, *Observatory*, 99, 128
- Efremov, Yu. N. 1998, *Astronomical & Astrophysical Transactions*, 15, 3
- Elmegreen, B. G. 1982, *ApJ*, 253, 634

Elmegreen, B. G. 1982, ApJ, 253, 655

Elmegreen, B. G. 1987, ApJ, 312, 626

Elmegreen, B. G. 1992, in *The Galactic Interstellar Medium (SAAS-FEE course)*, ed. D. Pfenniger & P. Bartholdi, (New York: Springer), 157

Elmegreen, B. G. 1993, in *Star Formation, Galaxies and the ISM*, ed. J. Franco, F. Ferrini & G. Tenorio-Tagle, (Cambridge: Cambridge U. Press), 335

Elmegreen, B. G., & Elmegreen, D. M. 1983, MNRAS, 203, 31

Elmegreen, B. G. & Elmegreen, D. M. 1986, ApJ311, 554

Elmegreen, B. G., & Elmegreen, D. M. 1987, ApJ, 320, 182

Franco, J., Santillán, A., & Martos, M. A. 1995, in *Formation of the Milky Way*, ed. E. J. Alfaro & A. J. Delgado (Cambridge: Cambridge Univ. Press), 97

Grabelsky, D. A., Cohen, R. S., Bronfman, L., & Thaddeus, P. 1988, ApJ, 331, 181

Hanasz, M. & Lesch, H. 2000, ApJ, 543, 235

Heiles, C. 1996, in *ASP Conf. Ser. 97, Polarimetry of the Interstellar Medium*, ed. W. G. Roberge & D. C. B. Whittet, (San Francisco: ASP), 457

Hughes, D. W., & Cattaneo, F. 1987, *Geophys. Astrophys. Fluid Dynamics*, 39, 65

Indrani, C., & Deshpande, A. A. 1998, *New Astronomy*, 4, 33

Jackson, J. M., Bania, T. M., Simon, R., Clemens, D. P., & Heyer, M. H. 2001, ApJ, submitted

Kim, J., Franco, J., Hong, S. S., Santillán, A., & Martos, M.A. 2000, ApJ, 531, 873 (Paper I)

- Kim, J., & Hong, S. S. 1998, ApJ, 507, 254
- Kim, J., Hong, S. S., Ryu, D., & Jones, T. W. 1998, ApJ, 506, L139
- Kim, J., & Ryu, D. 2001, ApJ, in press
- Kim, J., Ryu, D., & Jones, T. W. 2001, ApJ, 557, 464
- Kim, J., Ryu, D., Jones, T. W., & Hong, S. S. 1999, ApJ, 514, 506
- Lee, S. M., & Hong, S. S. 2001, in preparation
- Liszt, H. S. 1985, The Milky Way Galaxy, IAU Symp. 106, (Dordrecht: Reidel), 283
- Maddalena, R. & Thaddeus, P. 1984, ApJ, 294, 231
- Malhotra, S. 1994, ApJ, 433, 687
- Malhotra, S. 1995, ApJ, 448, 138
- Martos, M. A., & Cox, D. P. 1998, ApJ, 509, 703
- Martos, M., Allen, C., Franco, J., & Krutz, S. 1999, ApJ, 526, L89
- Masset, F., & Tagger, M. 1996, A&A, 307, 21
- Masset, F., & Tagger, M. 1997, A&A, 318, 747
- Minter, A., Lockman, F. J., Langston, G. L & Lockman, J. A. 2001, astro-ph/0101115
- Mouschovias, T., Shu, F. & Woodward, P. 1974, AA, 33, 73
- Parker, E. N. 1966, ApJ, 145, 811
- Parker, E. N. 1967, ApJ, 149, 535

- Roberts, D. A. & Burton, W. B. 1997, "Topics in Interstellar Matter", ed. H. van Woerden, (Dordrecht: Reidel), 195
- Santillán, A., Franco, J., Martos, M., & Kim, J. 1999, *ApJ*, 515, 657
- Santillán, A., Kim, J., Franco, J., Martos, M., Hong, S. S., & Ryu, D. 2000, *ApJ*, 545, 353
(Paper II)
- Schmidt-Kaler, Th., & Schlosser, W. 1973, *A&A*, 25, 191
- Shu, F. 1974, *AA*, 33, 55
- Simon, R., Jackson, J.M., Clemens, D. P., & Bania, T. M. 2001, *ApJ*, 551, 747
- Spicker, J., & Feitzinger, J. V. 1986, *A&A*, 163, 43
- Vallee, J. P. 1998, *Fundamentals of Cosmic Physics*, 19, 1
- Williams, J.P., & Maddalena, R. 1996, *ApJ*, 464, 247

Figure Captions

Fig. 1.— The run of the rms velocities as a function of time. The natural log is used along the ordinate. The solid line has a slope equal to the growth rate for the fastest growing undular mode. The units of velocity and time are the isothermal sound speed, 8.4 km sec^{-1} , and sound crossing time over the effective scale height, $1.5 \times 10^7 \text{ yr}$, respectively.

Fig. 2.— Perspective views of density structures, velocity vectors, and magnetic field lines at three selected times: $t = 15, 25,$ and 32 . Again, the time unit is $1.5 \times 10^7 \text{ yr}$. The computational box (4 kpc)³ is oriented in such a way that the radial (x), azimuthal (y), and vertical (z) directions are from left to right, from near to far, and from bottom to top, respectively. Color-coded densities are plotted in the central (x, z) plane. Colors are mapped from red to purple as density decreases. The velocity vectors are represented by red arrows, and the velocity unit is rescaled at each time. The maximum velocity vectors in the three frames are $6.47, 49.73,$ and $41.33 \text{ km sec}^{-1}$, respectively. Two isodensity surfaces, with the reference density $n = 0.04 \text{ cm}^{-3}$, are also shown above and below the midplane. Thirty-two field lines, whose starting points lie along a vertical line in the front (x, z) plane, are plotted as blue tubes.

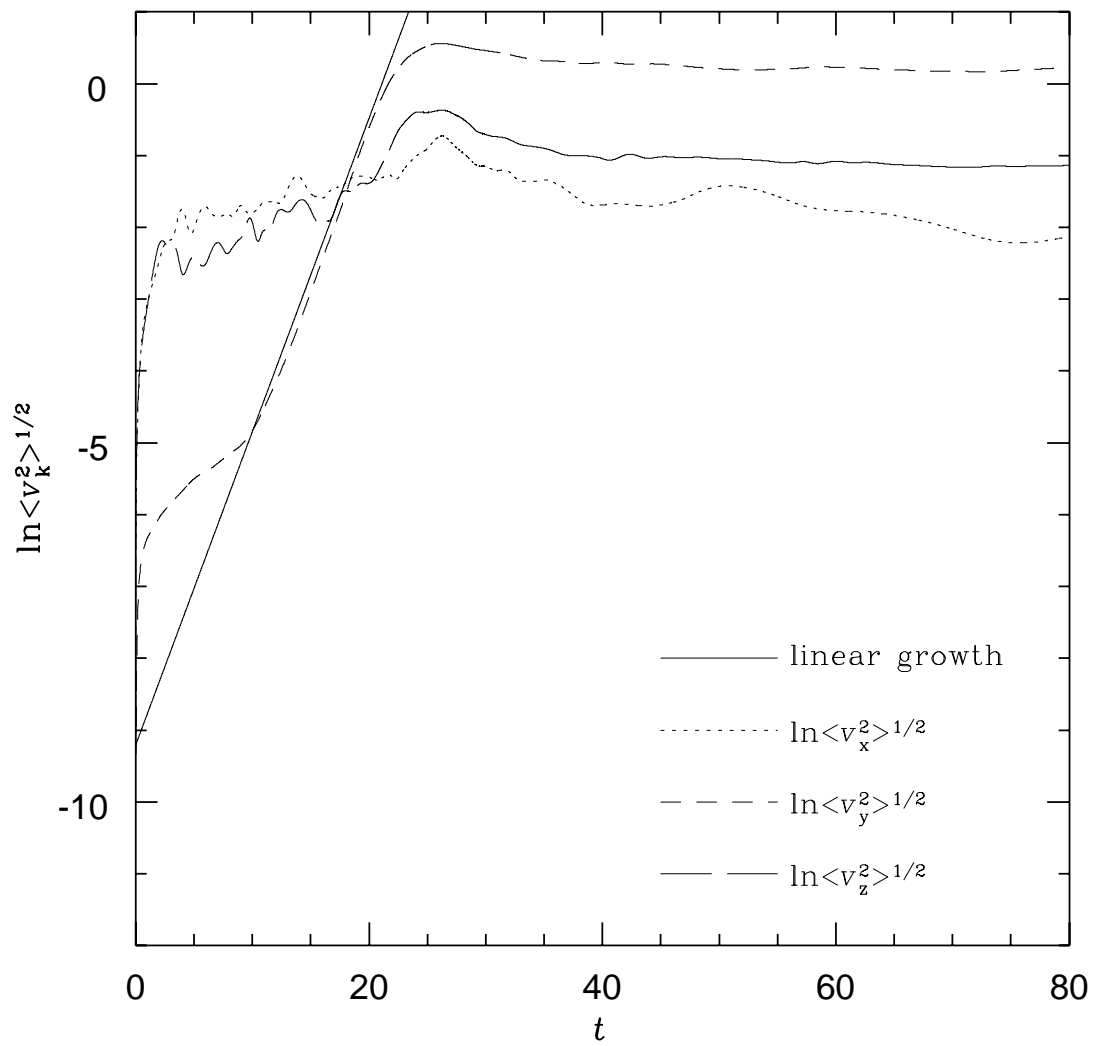
Fig. 3.— Column density maps, integrated along the z -axis from -2 kpc to $+2 \text{ kpc}$, for the same selected times displayed in Fig. 2. The column density values are normalized to the initial value, $1.1 \times 10^{21} \text{ cm}^{-2}$. Thick solid lines with this initial value separate the under-dense and over-dense regions. The thin solid (dotted) lines show normalized column densities larger (smaller) than 1.0, and the interval between successive lines is 0.1. A gray scale image is also overlaid, to provide a better representation of the over-dense and under-dense regions. The time and length units are $1.5 \times 10^7 \text{ years}$ and kpc , respectively.

Fig. 4.— Sliced density maps at $t = 32$. (a) The left panel represents a gray image densities

on the (x, y) plane, together with isodensity contours. Density levels are from 0.4 to 1.2 with 0.2 interval. A cubic-polynomial fitting curve that passes through the peaks of the main condensations along the spiral arm is also included. (b) The right panel represents a gray image of the vertical density distribution along the curve of the left panel superposed on isodensity contours. The units of time, length and density are 1.5×10^7 yr, kpc, and 1.4 cm^{-3} (a midplane value), respectively.

Fig. 5.— Magnetic field lines near the central (a) (y, z) and (b) (x, y) planes, together with isodensity surfaces with $n = 0.8 \text{ cm}^{-3}$ at $t = 32$. Again, the time unit is 1.5×10^7 yr.

Fig. 6.— Position-velocity map along the spiral arm. This figure shows an important kinematic signature of the process, The positions run along the curve defined in Figure 4a, and the velocity corresponds to the z -component at $t = 32$. The time unit is 1.5×10^7 yr.



This figure "franco-2a.jpg" is available in "jpg" format from:

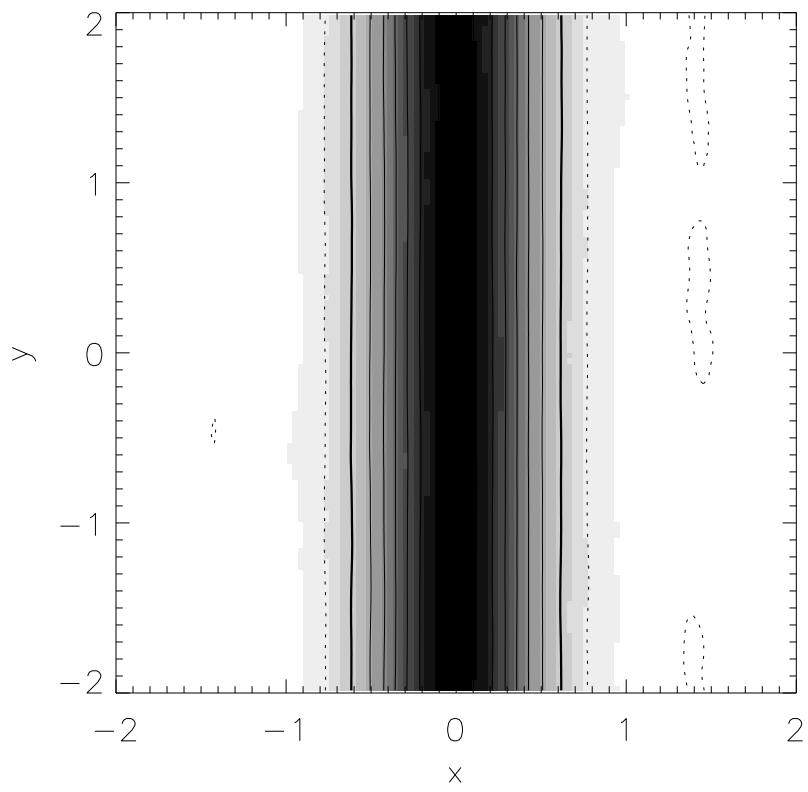
<http://arxiv.org/ps/astro-ph/0111406v1>

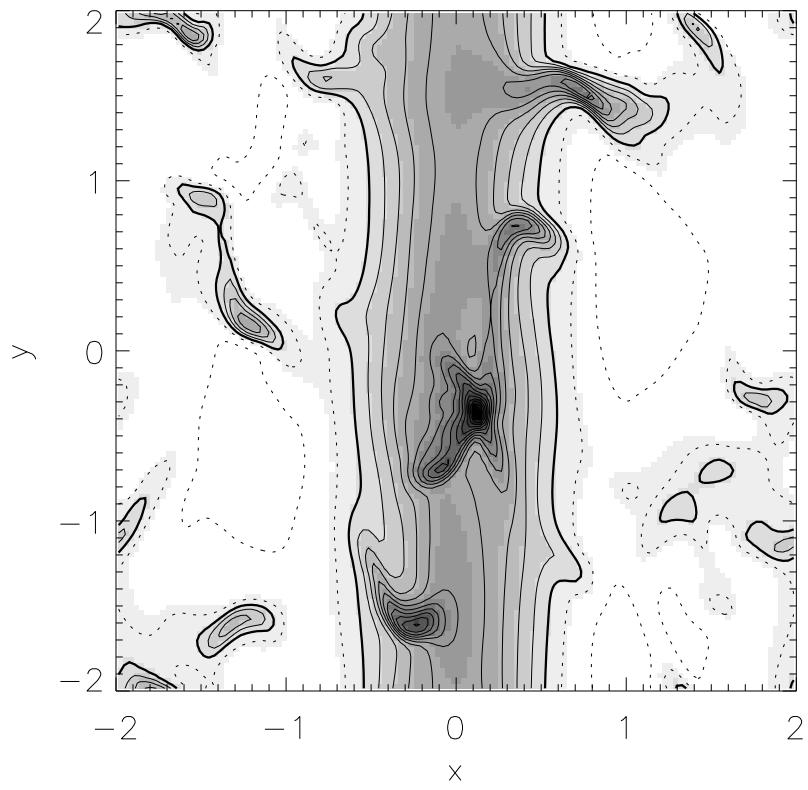
This figure "franco-2b.jpg" is available in "jpg" format from:

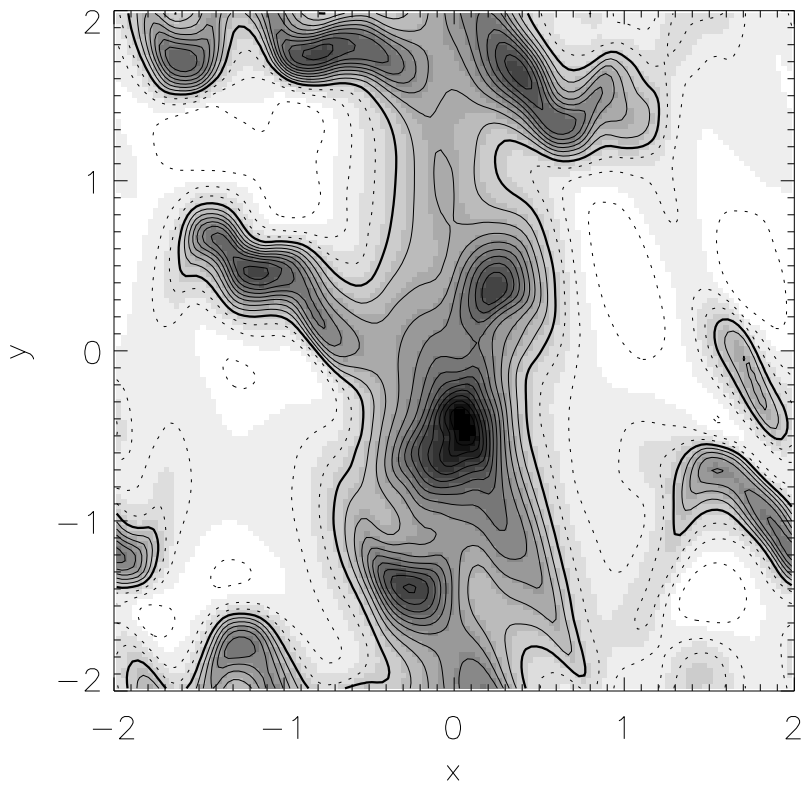
<http://arxiv.org/ps/astro-ph/0111406v1>

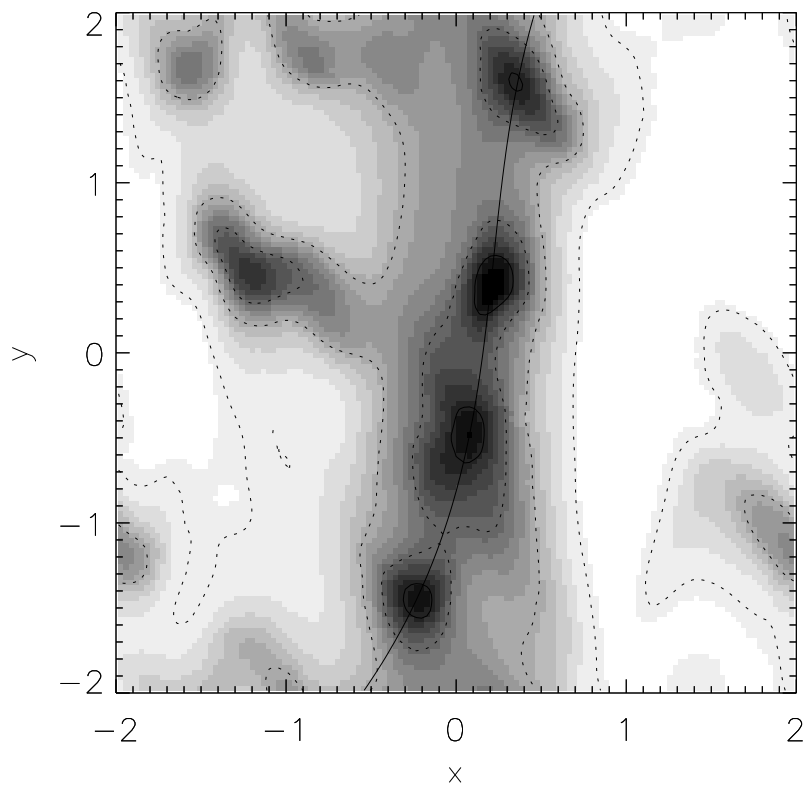
This figure "franco-2c.jpg" is available in "jpg" format from:

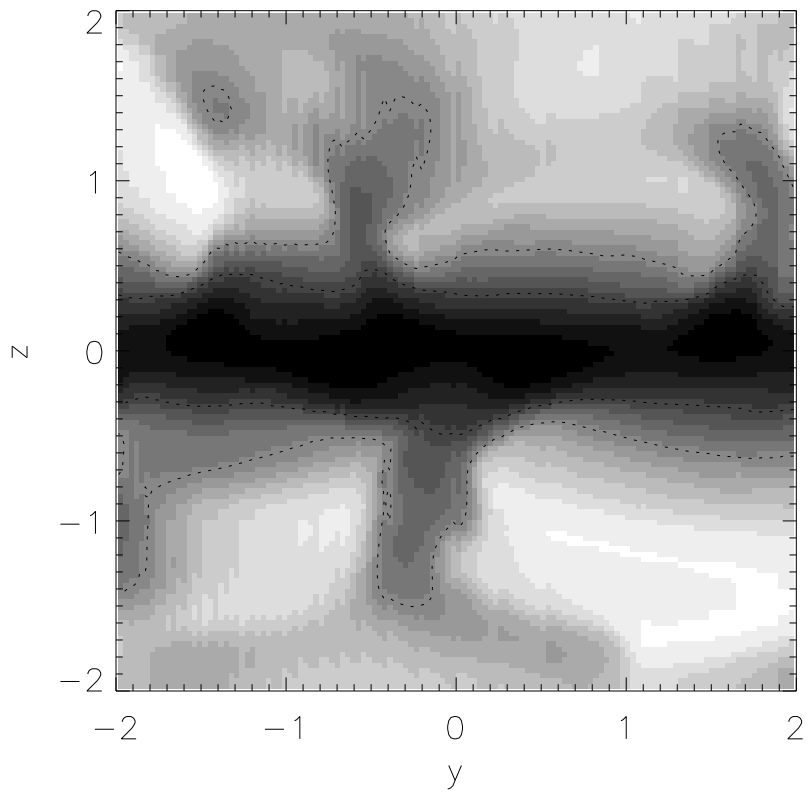
<http://arxiv.org/ps/astro-ph/0111406v1>











This figure "franco-5a.jpg" is available in "jpg" format from:

<http://arxiv.org/ps/astro-ph/0111406v1>

This figure "franco-5b.jpg" is available in "jpg" format from:

<http://arxiv.org/ps/astro-ph/0111406v1>

